

Article

Effect of Dose Rate on Tribological Properties of 8Cr4Mo4V Subjected to Plasma Immersion Ion Implantation

Bin Miao ^{1,2,*}, Junbo Niu ², Jiaxu Guo ², Zifeng Ding ², Xinghong Zhang ^{2,3}, Xinxin Ma ^{1,2,*} and Liqin Wang ⁴¹ State Key Laboratory of Advanced Welding and Joining, Harbin Institute of Technology, Harbin 150001, China² School of Materials Science and Engineering, Harbin Institute of Technology, Harbin 150001, China;

19b309009@stu.hit.edu.cn (J.N.); jxguo_hit@163.com (J.G.); dzf1163038669@163.com (Z.D.);

zhxh710@126.com (X.Z.)

³ AECC Harbin Bearing Co., Ltd., Harbin 150001, China⁴ MIIT Key Laboratory of Aerospace Bearing Technology and Equipment, Harbin Institute of Technology,

Harbin 150001, China; lqwang@hit.edu.cn

* Correspondence: bingomiao@126.com (B.M.); maxin@hit.edu.cn (X.M.)

Abstract: The lack of service lifetime of bearings has become a bottleneck that restricts the performance of aero engines. How to solve or improve this problem is the focus of most surface engineering researchers at present. In this study, plasma immersion ion implantation was conducted; in order to enhance the ion implantation efficiency and improve the wear resistance of 8Cr4Mo4V bearing steel, the dose-rate-enhanced method was adopted during ion implantation. The surface roughness, phase constituents, elemental concentration, hardness, contact angle and wear resistance of samples after ion implantation was determined by atomic force microscopy (AFM), grazing incidence X-ray diffraction (GIXRD), elemental dispersive spectroscopy (EDS), X-ray diffraction, nanoindentation tester, universal friction and wear tester, etc. The results showed that the high-dose-rate method had a significant enhancement influence on ion implantation efficiency. At the dose rate of 2.60×10^{17} ions/cm²·h, the roughness of Ra decreases from 24.8 nm to 10.4 nm, which is decreased by 58.1% for the dose rate of 7.85×10^{17} ions/cm²·h. XRD confirmed that the implanted samples consisted of the Fe(M) and Fe₂₋₃N phase and CrN which depends on the implantation dose rate. Meanwhile, the surface hardness was improved from 11.1 GPa to 16.9 GPa and enlarged the hardened region; more valuably, the surface state of samples via high-dose-rate implantation exhibits hydrophobicity with high roughness which is able to store debris and decrease the abrasive wear during testing; thereby, the wear resistance was greatly enhanced by high-dose-rate plasma immersion ion implantation.

Keywords: 8Cr4Mo4V steel; nitrogen ion implantation; plasma immersion ion implantation; dose-rate; wear resistance



Citation: Miao, B.; Niu, J.; Guo, J.; Ding, Z.; Zhang, X.; Ma, X.; Wang, L. Effect of Dose Rate on Tribological Properties of 8Cr4Mo4V Subjected to Plasma Immersion Ion Implantation. *Processes* **2024**, *12*, 190. <https://doi.org/10.3390/pr12010190>

Academic Editor: Prashant K. Sarswat

Received: 9 November 2023

Revised: 25 December 2023

Accepted: 6 January 2024

Published: 15 January 2024



Copyright: © 2024 by the authors. Licensee MDPI, Basel, Switzerland. This article is an open access article distributed under the terms and conditions of the Creative Commons Attribution (CC BY) license (<https://creativecommons.org/licenses/by/4.0/>).

1. Introduction

As a quintessential high-temperature bearing steel, 8Cr4Mo4V is usually characterized by its high concentrations of chromium (Cr) and molybdenum (Mo) alloys. This steel is renowned for its exceptional properties, including superior tempering resistance, remarkable high-temperature strength, excellent thermal stability and enhanced resistance to rolling contact fatigue and corrosion [1–10]. These attributes make 8Cr4Mo4V steel an ideal choice for the bearings in the main shafts of jet and gas turbine engines. As a result of these advantageous properties, its utilization in both industrial and aerospace applications has significantly increased [11–21].

Through conventional martensitic quenching, the surface hardness of 8Cr4Mo4V steel can attain 60–64 HRC. This process primarily hinges on the secondary hardening effect during later high-temperature tempering [13,22–24], giving 8Cr4Mo4V notable strength and resistance to contact fatigue [25–31]. Unfortunately, bearings in aerospace applications are subjected to harsh environmental conditions, marked by extreme temperatures, elevated

contact pressures and exposure to vacuum and radiation [14]. These challenging conditions present formidable challenges to the durability and broader application of these bearings. In such demanding environments, the surface condition of the materials becomes critically important. It influences not only the service lifespan of the bearings but also impacts the other key material properties, such as tribological performance.

Ongoing global scientific research on advanced materials has led numerous groups to push material performances beyond theoretical limits, aiming to achieve optimal results [32]. When the direct manipulation of raw materials is challenging, surface modification emerges as a robust strategy to enhance both performance and durability, particularly for materials subjected to harsh environments or extreme conditions. To enhance surface properties, various advanced surface modification techniques have been developed, including plasma or gas nitriding [33,34], magnetron sputtering [35], and ion implantation [36].

Plasma immersion ion implantation and plasma nitriding are both advanced surface modification techniques that utilize plasma to enhance the properties of materials. In plasma immersion ion implantation, ions from the plasma are directly implanted into the surface of the material. It allows for the implantation of ions into complex geometries and non-line-of-sight areas, and it offers a more uniform implantation over the entire surface. Meanwhile, it can achieve higher concentrations of nitrogen on the surface, enhancing the hardness and wear resistance. Plasma immersion ion implantation serves effectively as the final step in the manufacturing process, preserving the dimensional precision of the workpiece. Its advantage lies in creating a shallow implanted layer, which significantly reduces the risk of contact fatigue originating from the surface. Conversely, plasma nitriding, although it has the distinct advantage of prolonging the service life against contact fatigue, suffers high-temperature treatment that may cause considerable deformation, necessitating further grinding. The process may result in less control over the uniformity of the nitrided layer, especially in complex-shaped objects.

Both processes are able to improve the surface hardness, wear resistance and fatigue life without significant distortion of the material. The choice between plasma immersion ion implantation and plasma nitriding would depend on the specific application requirements, including the desired depth and concentration of nitrogen, the geometry of the parts and economic considerations.

For several decades, plasma immersion ion implantation has emerged as a significantly attractive technique for the surface modification of metallic materials. This method is particularly notable for its ability to enhance the wear resistance of bearings under severe conditions. It achieves this by infusing atomic nitrogen into the surfaces of components, a process that improves their properties without altering the surface finish. However, a notable limitation of the current plasma immersion ion implantation techniques is their time-consuming nature, often requiring dozens of hours or more to achieve the desired material properties. This makes the process energy-intensive and relatively inefficient [37–39]. In response to these challenges, there is growing interest in the development of high-dose-rate ion implantation methods, which promise to offer more efficient processing solutions. To our knowledge, scant studies have addressed the effect of high dose rates on plasma immersion ion implantation for 8Cr4Mo4V bearing steel [1,9,40]. Furthermore, enhancing the friction and wear behaviors of 8Cr4Mo4V steel and boosting implantation efficiency are pressing concerns demanding more research. Additionally, the correlation between high-dose-rate implantation and tribological performance remains elusive, underscoring the importance of studying the impact of implantation dose rate on 8Cr4Mo4V bearing steel.

After going through the extensive literature, it is observed that limited work can be found for analyzing the high-dose-rate plasma immersion ion implantation impact on 8Cr4Mo4V bearing steel, and the effect of high-dose-rate ion implantation on 8Cr4Mo4V is still unanswered. Hence, in this work, the high-dose-rate treatment on plasma immersion ion implantation with nitrogen ions is conducted, and the detailed grazing incidence X-ray diffraction, the atomic force microscopy, elemental dispersive spectroscopy, nanoinden-

tation tester and universal friction and wear tester analysis are utilized to investigate the effect of high-dose-rate ion implantation on tribological properties of 8Cr4Mo4V steel. The experimental results will be useful for structural scientists and engineers and prompt the practical application of plasma immersion ion implantation in intelligent manufacturing.

2. Experimental Details

The material studied is 8Cr4Mo4V (AISI M50) steel, its specific chemical composition is listed in Table 1, and supplied by Fushun Special Steel Co., Ltd., Fushun, China. The quenched and tempered as-received steel owns an initial nanohardness of 11.1 GPa.

Table 1. Chemical composition of 8Cr4Mo4V steel (wt.%).

C	Cr	Mo	V	Ni	Mn	Si	Co	W	Fe
0.80~0.85	4.00~4.25	4.00~4.50	0.90~1.10	≤0.15	0.15~0.35	≤0.25	≤0.25	≤0.25	Bal.

The experiments of plasma immersion ion implantation were performed with a DLZ-01 PBII apparatus independently developed by the Harbin Institute of Technology of China, which was illustrated in Figure 1 and detailed in reference [36]. The equipment has a pulse voltage output range of 5–100 kV (pulse width can be adjusted), a maximum average output current of 100 mA, and a maximum peak output current of 50 A. The chamber body is connected to the grounded potential serving as an anode. The sample holder is seamlessly integrated with the power supply serving as the cathodic plate. Additionally, the setup incorporates an oscilloscope and computer interface that interacts with the equipment, facilitating the real-time observation and analysis of voltage and current parameters throughout the treatment process.

Flat specimens of 8Cr4Mo4V bearing steel, each with a thickness of 4.5 mm and a diameter of 16.5 mm, were meticulously prepared for comprehensive structural analysis and precise measurement of mechanical properties.

The initial samples underwent mechanical polishing using SiC abrasive papers (grit sizes 180# to 2000#), followed by a final polish with diamond grit paste to achieve a mirror finish. The samples were cleaned ultrasonically with ethanol for 30 min before implantation. The vacuum system was thoroughly evacuated to achieve a base pressure below 2.0×10^{-3} Pa. Subsequently, it was carefully back-filled with nitrogen adjusting to a working pressure of 0.3 Pa while maintaining a controlled gas flow rate of 30 sccm.

Ultimately, nitrogen ion implantation was carried out at ambient temperature, utilizing an acceleration energy of 20 keV. This process was uniformly applied across various implantation dose rates, specifically 2.60×10^{17} , 5.18×10^{17} , 7.85×10^{17} , and 1.04×10^{18} ions/cm²·h, all while maintaining a consistent implantation dose of 2.215×10^{20} ions/cm², classified as a high dose. Under the premise of maintaining a consistent nitrogen ion implantation dose, we have the capability to regulate the dose rate by adjusting various experimental parameters. These adjustments include, but are not limited to, modifications in pulse width and frequency. In this instance, we specifically altered the frequency range, shifting it from 1000 Hz to 5000 Hz.

Simultaneously, the identical dimensions of GCr15 and 8Cr4Mo4V steel samples were affixed to the implantation device. This setup guaranteed uniform temperature conditions for both samples throughout the treatment process. The temperature was meticulously determined based on the Rockwell hardness of the implanted GCr15 steel and subsequently calculated using a scientifically established equation, as referenced in [41].

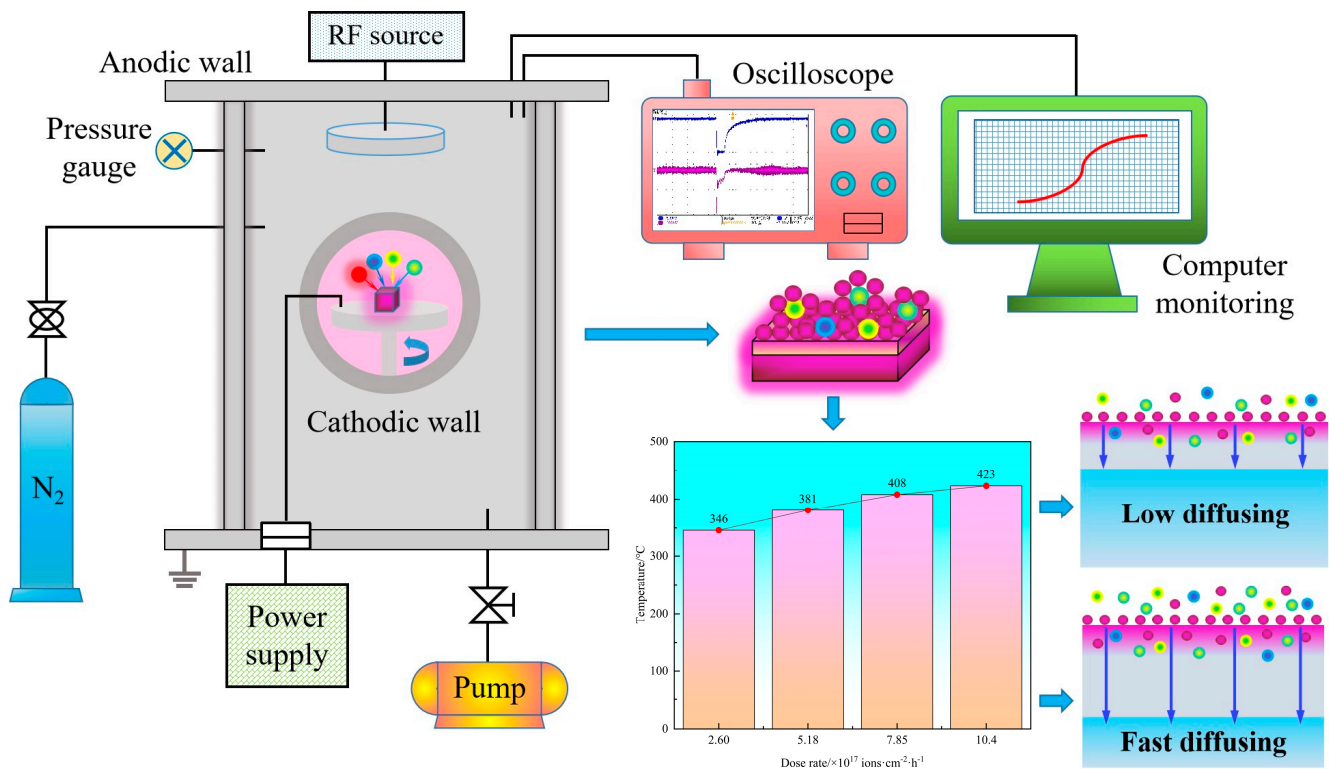


Figure 1. The schematic diagram of setup utilized in plasma immersion ion implantation.

During the process of high-dose-rate implantation, the surface undergoes activation due to relentless ion bombardment. This activity among surface atoms is further amplified by interactions with high-energy ions. Such intense bombardment invariably leads to an increase in temperature over the course of the treatment, thereby influencing and altering the diffusion rates.

Microstructural observations of the samples were conducted using a ZEISS SUPRA55 scanning electron microscope (SEM), which has a high resolution (1.7 nm at 1 kV; 1.0 nm at 15 kV), high magnification (12–900,000 times), and accelerating voltage of 20 kV were used. It provides nanoscale compositional analysis and imaging on the examined substrates. The chemical composition was determined using energy dispersive spectroscopy (EDS) integrated with the SEM.

A Park System designed atomic force microscope (AFM), KANC 4F, was utilized to examine the 3D morphology of the implanted surface. Grazing incidence X-ray diffraction (GIXRD) utilizing Cu-K α radiation ($\lambda = 1.54056 \text{ \AA}$) was applied to study the microstructural alterations resulting from nitrogen ion implantation.

The hardness distribution was meticulously evaluated using nanoindentation experiments, conducted with an MTS nano-indenter. For these assessments, a Berkovich diamond indenter, characterized by a 20 nm radius of curvature at its apex was employed. This was conducted in the context of Continuous Stiffness Measurements (CSM), maintaining a uniform indentation depth of 1 μm throughout the process.

Contact angles associated with distilled water and formamide droplets on the examined surface were accurately determined using a JC2000D1 system, operating under ambient temperature conditions. The precision of these measurements is reflected in the minimal error margin, which is maintained within 3%.

These measurements facilitated the calculation of the surface free energy (SFE) for the implanted surface. Droplets, each having a volume of 20 mm^3 were dispensed onto the sample surfaces using a micropipette. A minimum of three droplets were placed on each specimen. Contact angles for each droplet were then measured on both sides. And finally, the value of SFE was calculated by Equations (3)–(5).

Tribological properties were evaluated using a CETR-UMT ball-on-disk wear tester during dry sliding. The test conditions comprised a 1.16 N load, 120 rpm rotation rate, and opposition by a WC ball with a 5.5 mm diameter, with each test lasting 600 s. Wear tests were conducted at an ambient temperature of $20 \text{ }^\circ\text{C}$ and an approximate relative humidity of 40%. To ensure repeatability, each test was repeated thrice.

The worn volume (V) of the specimens was meticulously calculated in accordance with the ASTM G99-04 standard, as referenced in [42]:

$$V = \frac{\pi \cdot r_w \cdot w^3}{6 \cdot r_p} \quad (1)$$

In this formula, V represents the worn volume (in mm^3), r_w is the radius of the wear track (in mm), w denotes the width of the track (in mm), and r_p is the radius of the pin sphere (in mm).

Subsequently, the specific wear rate was derived using Equation (2), as outlined in [43]:

$$W = V/SF \quad (2)$$

In this context, W signifies the wear rate ($\text{mm}^3 \cdot \text{N}^{-1} \cdot \text{m}^{-1}$), and V denotes the worn volume (mm^3). F represents the applied load (N), and S indicates the sliding distance (m). Additionally, the width of the wear tracks was ascertained through analysis of surface images captured post-wear test.

3. Results and Discussions

3.1. Surface Roughness of the Surface Layer Treated by High-Dose-Rate Ion Implantation

Figure 2 reveals the AFM micrographs of implanted samples at various dose rates. Figure 2b,c reveal the prominent mountain-like micro-bulges on the outermost surface of samples implanted at dose rates of $2.60 \times 10^{17} \text{ ions/cm}^2 \cdot \text{h}$ and $5.18 \times 10^{17} \text{ ions/cm}^2 \cdot \text{h}$. When the steel is subjected to nitrogen ion implantation at the dose rate of $7.85 \times 10^{17} \text{ ions/cm}^2 \cdot \text{h}$, the prevalence of micro-bulges appears to diminish, giving way to smaller mountain-like features and the emergence of deep holes. AFM measurements, as indicated in Figure 2f, also reveal the roughness of the implanted samples. Compared to the original sample, there is an observed increase in surface roughness for the steel implanted by various dose rates. This phenomenon is primarily attributed to high-energy ion collisions during implantation, leading to the introduction of numerous defects, radiation damage, and associated sputtering. Considering the combined influence of high-dose-rate ion implantation, the surface roughness increases accordingly. As compared to the implanted samples at the dose rate of $2.60 \times 10^{17} \text{ ions/cm}^2 \cdot \text{h}$ and $7.85 \times 10^{17} \text{ ions/cm}^2 \cdot \text{h}$, the obtained results show that the value of R_q decreases from 32.2 nm to 13.8 nm, and R_a decreases from 24.8 nm to 10.4 nm, respectively. The observed smoother surface is primarily attributed to the sputtering effects impacting the surface layer atoms. This sputtering results from collisions between the incident ions and recoil atoms in the vicinity of the sample's surface, as detailed in [44]. As can be seen in Figure 2f, the evolution trend of roughness initially decreases and then increases with the implantation dose rate. This increase in surface roughness may be due to changes in lattice parameters, particularly the augmented formation of dislocation density, during the high-dose-rate implantation process [41,44]. The values of R_q and R_a tend to rise to 24.3 nm and 18.9 nm, respectively, as the treating temperature increases. Such alterations in surface morphology and roughness post-implantation are attributed to the enhanced formation of the iron nitrides phase, as reported in [45,46].

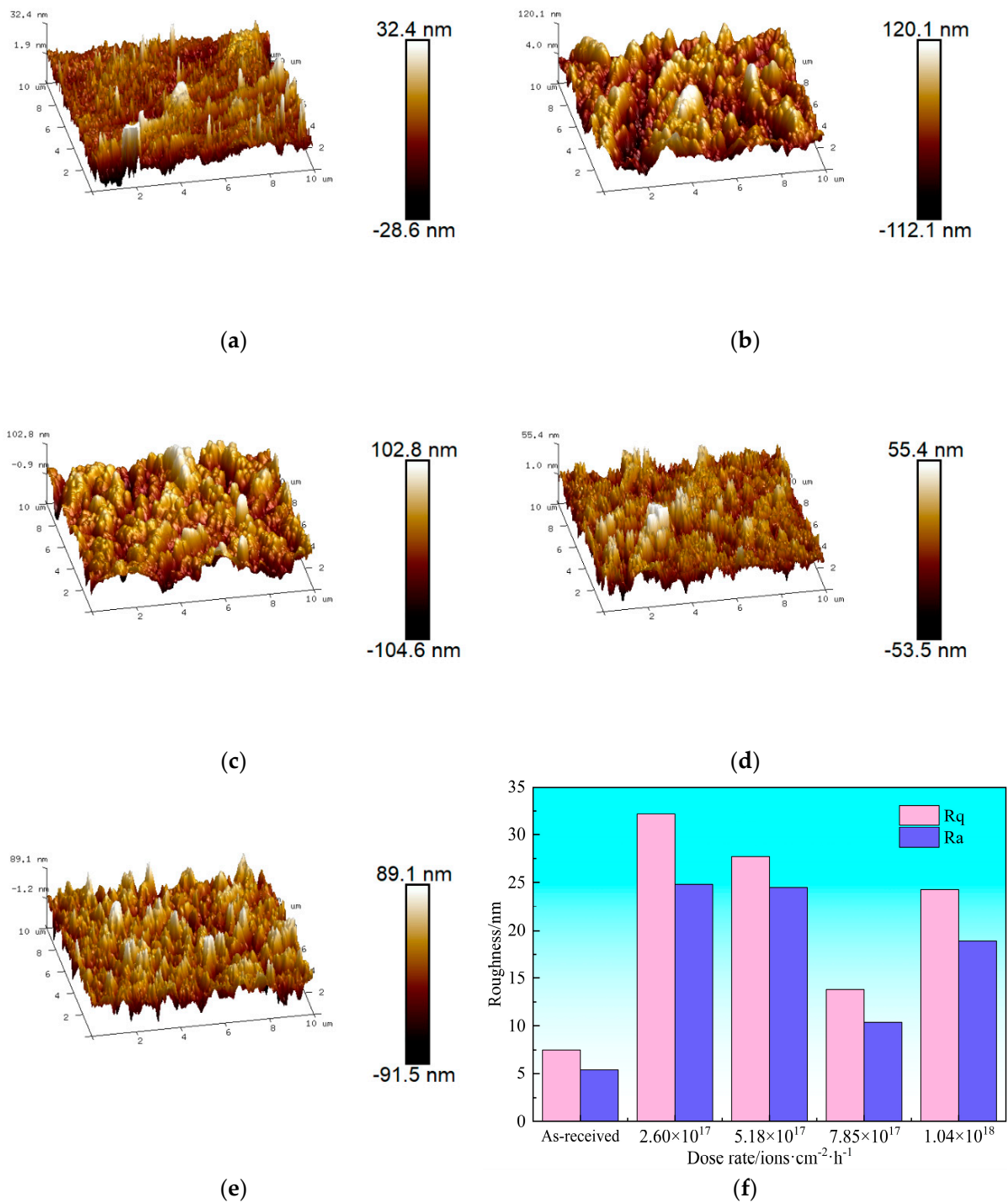


Figure 2. AFM images of 8Cr4Mo4V bearing steel implanted at various dose rate (a) as-received sample, (b) 2.60×10^{17} ions/cm²·h, (c) 5.18×10^{17} ions/cm²·h, (d) 7.85×10^{17} ions/cm²·h, (e) 1.04×10^{18} ions/cm²·h and roughness (f) measured by AFM.

3.2. Phase Composition of the Surface Layer Treated by High-Dose-Rate Ion Implantation

In order to gain a further understanding of the influence of dose rate, XRD was measured at different angles. Figure 3 depicts the phase composition of the implanted layer treated by various implantation dose rates. In our previous research study, the diffraction peak is composed of Fe(M) for the as-received sample [45]. For the samples that underwent ion implantation at a total dose of 2.215×10^{20} ions/cm², the new Fe₂₋₃N peaks emerged in the X-ray diffraction patterns. This was particularly notable at the high dose rate of

5.18×10^{17} ions/cm²·h ion implantation, as indicated in references [41,47]. Meanwhile, in comparison to the samples implanted at a dose rate of 1.04×10^{18} ions/cm²·h, those treated at dose rates ranging from 2.60×10^{17} to 7.85×10^{17} ions/cm²·h exhibited broadened diffraction peaks. Additionally, their peaks displayed a slight leftward shift by 0.777° . It is observed that the relative intensity of the Fe(M) peaks escalates with an increasing grazing angle. Notably, the slope of the grazing angle at 2° and 3° is more pronounced compared to the other angles. This phenomenon suggests that the high-dose-rate ion implantation leads to a partial substitution of nitrogen ions at the iron sites. Furthermore, during the ion implantation process, this high-dose-rate implantation is likely to cause changes in lattice parameters within the surface layer [41,46].

For the samples implanted at the same dose, in addition to the inherent effects of ion implantation, the implantation dose rate also plays a crucial role in influencing the differences in phase constituents. The GIXRD results clearly demonstrate that the nitrogen high-dose-rate implantation acts as a driving force, not only for the broadening and shifting of diffraction peaks but also for the formation of phases to a significant extent. However, the differences in the diffraction peaks broaden and shift and do not increase with the implantation dose rate; the presence of phases and new peaks suggest that there is an optimal implantation dose rate.

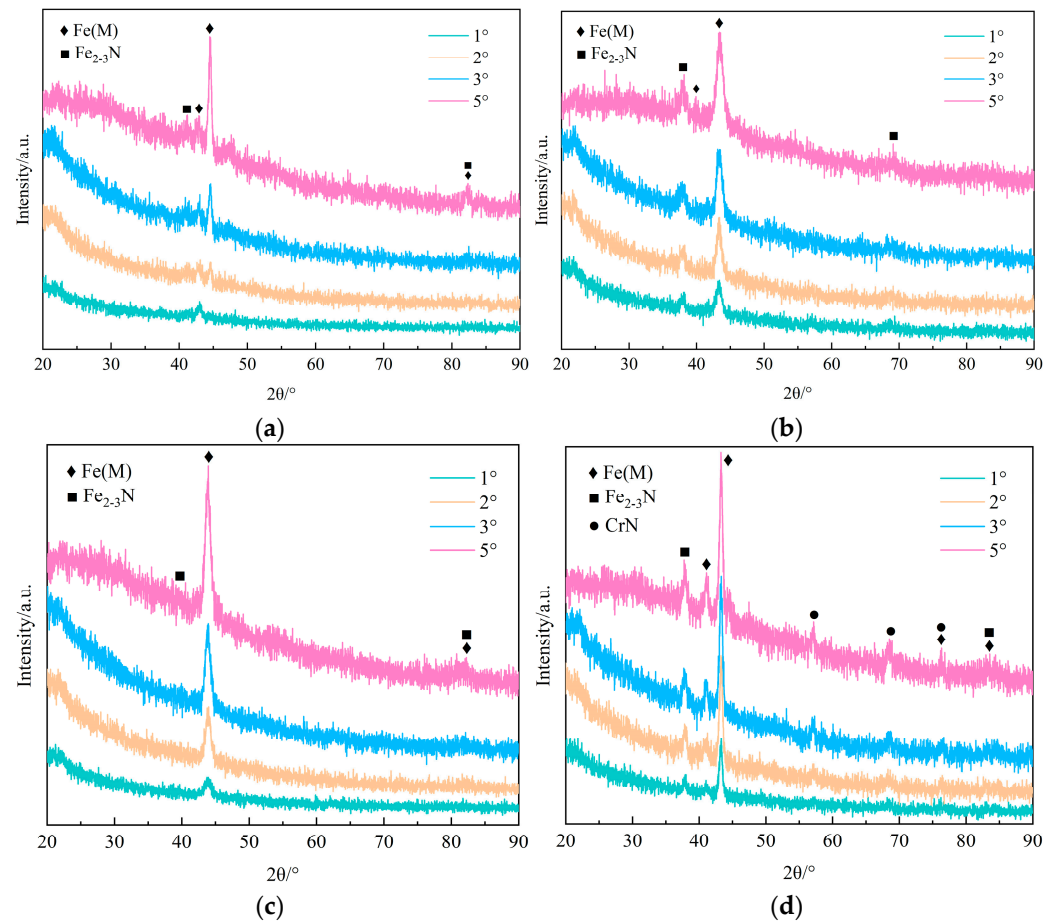


Figure 3. Cont.

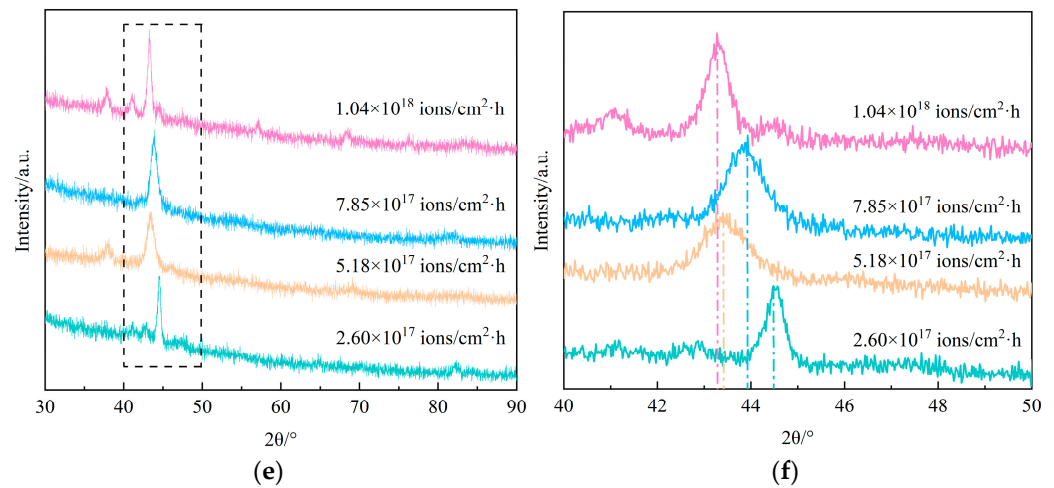


Figure 3. GIXRD patterns of the implanted layer under various implantation dose rates. (a) 2.60×10^{17} ions/cm²·h, (b) 5.18×10^{17} ions/cm²·h, (c) 7.85×10^{17} ions/cm²·h, (d) 1.04×10^{18} ions/cm²·h, (e) XRD patterns of the implanted layer under various implantation dose rates, (f) partial enlarged view of (e).

3.3. Elemental Percentage of the Surface Layer Treated by High-Dose-Rate Implantation

Figure 4 depicts the elemental percentage of the modified layer treated by various implantation dose rates. The weight % and atomic % of the respective elements contained in the implanted surface layer are listed in Table 2. As can be seen in Figure 4a and Table 2, it can be seen that the N concentration decreases from 10.0% to 1.3% and C concentration remains unchanged with the enhanced dose rates, and the Fe concentration initially remains at almost the same value of 70.4~71.9% when the dose rate is between 2.60×10^{17} and 7.85×10^{17} ions/cm²·h, while it increases to 84.7% when the dose rate reaches 1.04×10^{18} ions/cm²·h. From Figure 4b, it can be observed the same phenomena of N concentration decreases from 23.1% to 3.3%, and the Fe concentration initially is approximate and then increases from 41.3% to 55.8%. Meanwhile, the Cr, Mo and V concentration reaches the highest at the dose rate of 7.85×10^{17} ions/cm²·h and reaches the lowest at the dose rate of 1.04×10^{18} ions/cm²·h from Figure 4c,d. This phenomenon primarily arises from the elevated temperatures experienced during high-dose-rate ion implantation. Elevated temperatures suggest that the high-dose-rate implantation promotes considerable nitrogen diffusion [47,48].

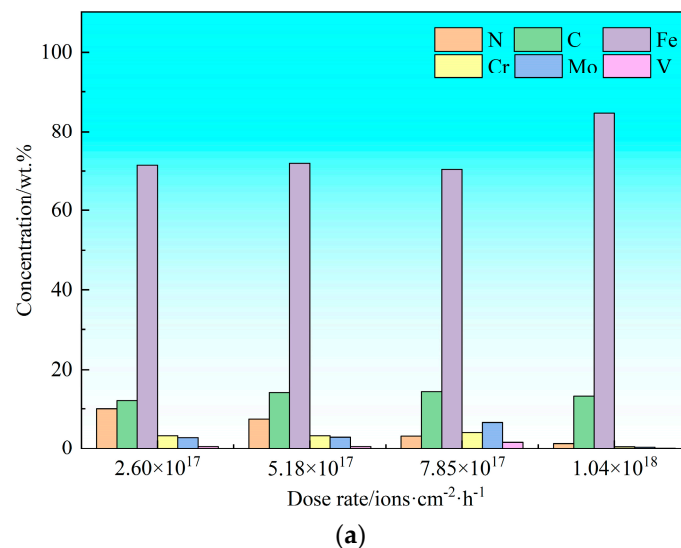


Figure 4. Cont.

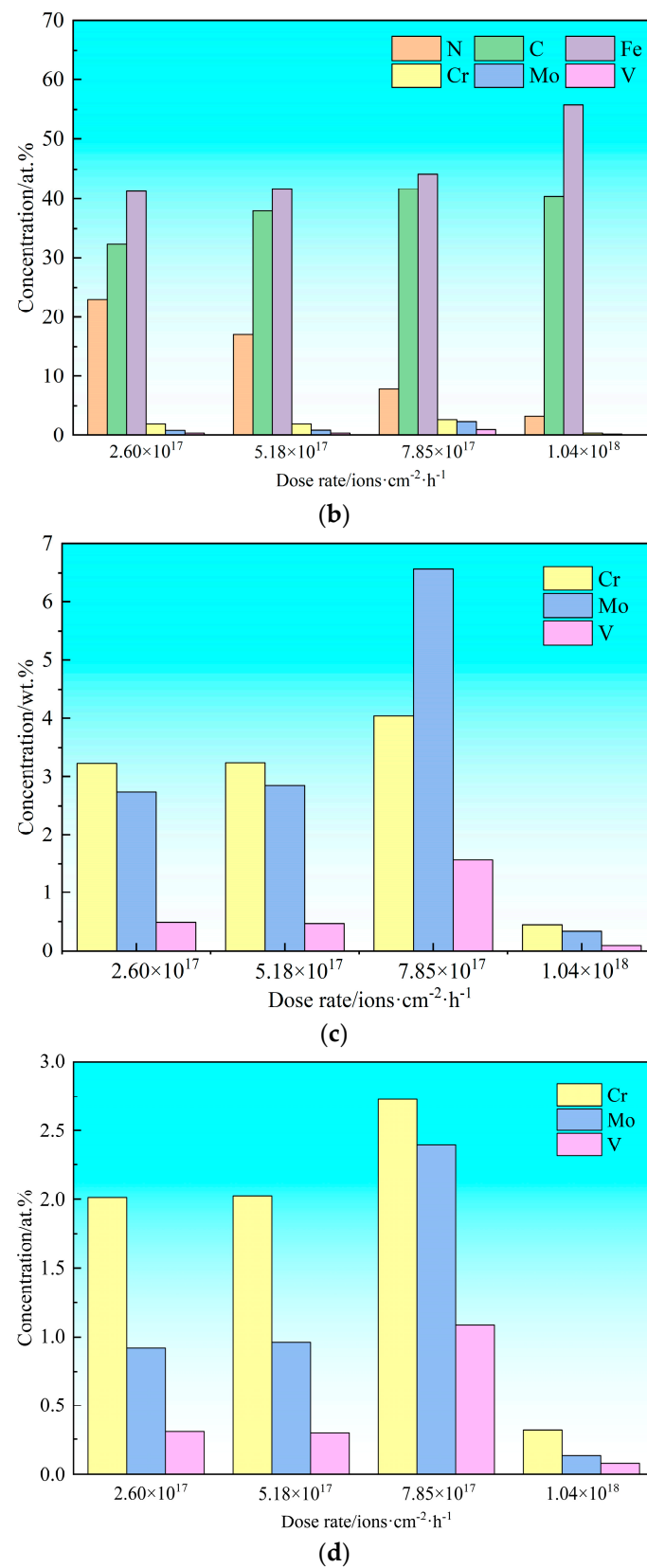


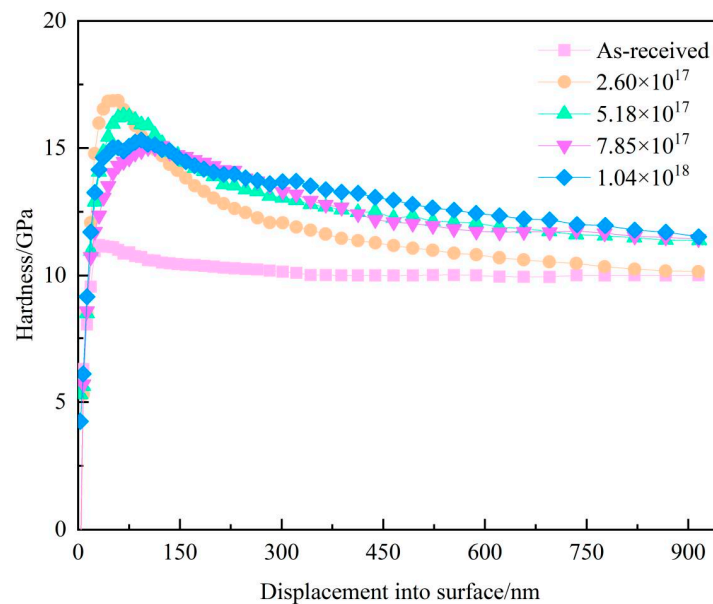
Figure 4. Elemental percentage of the implanted layer under various implantation dose rates. (a) mass percentage, (b) atomic percentage, (c) enlargement of Cr, Mo, V elements in mass percentage, (d) enlargement of Cr, Mo, V elements in atomic percentage.

Table 2. Elemental percentage of the implanted layer treated at various dose rates.

Dose rate (ions/cm ² ·h)	Elements											
	C Kα		N Kα		Fe Kα		Cr Kα		Mo Lα		V Kα	
	Wt %	At %	Wt %	At %	Wt %	At %	Wt %	At %	Wt %	At %	Wt %	At %
2.60×10^{17}	12.06	32.41	10.01	23.05	71.47	41.30	3.240	2.01	2.74	0.92	0.49	0.31
5.18×10^{17}	14.12	38.01	7.40	17.07	71.92	41.64	3.25	2.02	2.85	0.96	0.47	0.30
7.85×10^{17}	14.29	41.73	3.13	7.84	70.40	44.22	4.04	2.73	6.57	2.40	1.57	1.08
1.04×10^{18}	13.19	40.39	1.25	3.29	84.67	55.79	0.45	0.32	0.34	0.13	0.10	0.08

3.4. Nanohardness Analysis of the Surface Layer Treated by High-Dose-Rate Implantation

The characteristic hardness-displacement profiles of the samples implanted at various dose rates are shown in Figure 5. The surface hardness increases from 11.1 GPa to 16.9 GPa upon high-dose-rate ion implantation, representing a 52.3% enhancement compared to the non-implanted sample. The elevated surface hardness is crucial for improved wear resistance. Meanwhile, it is obvious that the samples via implantation dose rates of 5.18×10^{17} ions/cm²·h, 7.85×10^{17} ions/cm²·h, 1.04×10^{18} ions/cm²·h presents an enlarged hardened region in contrast to the samples after implantation dose rates of 2.60×10^{17} ions/cm²·h. This notable increase in hardness is primarily attributed to the formation of nitride phases and the emergence of extended defects within the crystalline structure. The high-energy incident ions contribute to the alterations in lattice parameters during the high-dose-rate implantation process. For the samples implanted at a dose rate of 5.18×10^{17} ions/cm²·h, the smallest grain size, along with the highest micro-strain and dislocation density were observed. These were quantified as 11.78 nm for grain size, 7.716×10^{-3} for micro-strain, and 1.559×10^{16} for dislocation density, respectively [41].

**Figure 5.** Nanoindentation of 8Cr4Mo4V steel implanted with various dose rates.

3.5. Contact Angles of the Surface Layer Treated by High-Dose-Rate Implantation

The apparent contact angles of the surface treated with and without high-dose-rate ion implantation are depicted in Figure 6. It can be seen that the contact angle of the non-implanted surface is 61.3° (the angle of the theoretical limit between hydrophilic and hydrophobic characteristics is 65°), which means that the non-implanted 8Cr4Mo4V steel is hydrophilic in nature. However, it can be observed that all the surfaces are hydrophobic after high-dose-rate ion implantation. For the implanted samples, the highest contact angle

value of 82.4° is obtained at the dose rate of 1.04×10^{18} ions/cm²·h. In contrast, the dose rate of 2.60×10^{17} ions/cm²·h, 5.18×10^{17} ions/cm²·h, and 7.85×10^{17} ions/cm²·h exhibit smaller contact angles of 81.9° , 78.2° , 76.8° , respectively.

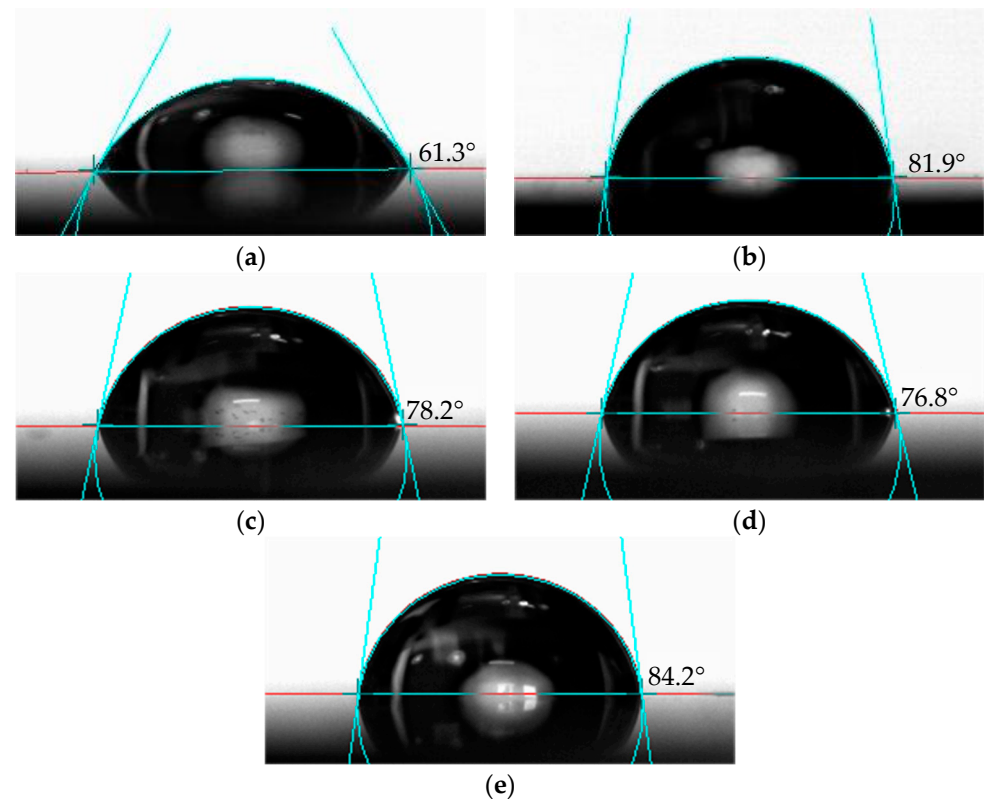


Figure 6. Optical images of 8Cr4Mo4V steel implanted at various dose rate. (a) As-received sample, (b) 2.60×10^{17} ions/cm²·h, (c) 5.18×10^{17} ions/cm²·h, (d) 7.85×10^{17} ions/cm²·h, (e) 1.04×10^{18} ions/cm²·h.

From the roughness results, it was found that the surface roughness plays a critical role in the wetting behavior at the liquid–solid interface with a decrease in the contact angle value with a decrease in the roughness for those implanted samples. Sarkar et al. [49] reported that the hydrophilicity and hydrophobicity are related to the solid surface roughness exponent. Compared to the mirror-finish non-implanted sample, the surface with a high roughness is expected to attract water when a water droplet is placed on the fractal surface. During the wear testing, the microstructure on the implanted surface can store debris and reduce the abrasive wear, thereby improving the wear resistance of the surface. Moreover, the contact angle values can be employed to calculate the surface free energy of the implanted surface layer.

3.6. Surface Free Energy of the Surface Layer Treated by High-Dose-Rate Implantation

The surface free energy (SFE) of the examined surface is detailed in Table 3. It has been computed by using the equation as specified in references [50,51]:

$$\gamma_s = \gamma_s^d + \gamma_s^p \quad (3)$$

In this context, γ_s , γ_s^d and γ_s^p represent the total, the dispersive and polar component of SFE, respectively. γ_s^d and γ_s^p can be accurately calculated using the Owens–Wendt method, as elaborated in references [50,51]:

$$\left(\gamma_s^d\right)^{1/2} = \frac{\gamma_f(\cos \theta_f + 1) - \gamma_w \sqrt{\gamma_f^p / \gamma_w^p} (\cos \theta_w + 1)}{2(\sqrt{\gamma_f^d} - \sqrt{\gamma_f^p \gamma_w^d / \gamma_w^p})} \quad (4)$$

$$\left(\gamma_s^p\right)^{1/2} = \frac{\gamma_w(\cos \theta_w + 1) - 2\sqrt{\gamma_s^d / \gamma_w^d}}{2\sqrt{\gamma_w^p}} \quad (5)$$

In this formulation, γ_f , γ_f^d and γ_f^p denote the SFE of formamide, along with its dispersive and polar components, respectively. Variables γ_w , γ_w^d and γ_w^p represent the SFE of deionized water and its corresponding dispersive and polar components. θ_w and θ_f correspond to the contact angle of deionized water and formamide, respectively.

Table 3. Contact angles and the SFE of 8Cr4Mo4V steel with high-dose-rate ion implantation.

Implantation Dose Rate (ions/cm ² ·h)	Contact Angles (°)		Surface Free Energy (mJ/m ²)						
	θ_w	θ_f	γ_f^d	γ_f^p	γ_w^d	γ_w^p	γ_s^d	γ_s^p	γ_s
2.60×10^{17}	81.9	69.9					15.3	45.3	61.4
5.18×10^{17}	78.2	68.3	39.0	19.0	21.8	51.0	14.7	47.2	61.9
7.85×10^{17}	76.8	65.4					16.2	48.8	65.3
1.04×10^{18}	82.4	73.5					12.8	41.6	54.4

Table 3 illustrates that the high-dose-rate implantation notably enhances the SFE, attributed to reduced contact angles. Surface energy is defined as the surface excess energy per unit area ($G_0 = \Delta G/A$), and is fundamentally determined by the excess energy on the surface (ΔG). Typically, an original steel surface is inert and exhibits low surface energy. However, surface modifications such as the incorporation of active nitrogen atoms can significantly elevate ΔG , as indicated in reference [51]. This increase in surface energy becomes evident when observing steel treated with varying ion implantation dose rates. Understanding the surface free energy of the implanted steels aids in effective surface treatments and modifications to enhance performance, such as improving adhesion, wetting properties, corrosion and wear resistance. In this research, it was found that the high surface free energy obtained at the dose rate of 7.85×10^{17} ions/cm²·h can help reduce the direct metal-to-metal contact, thereby decreasing the wear. The specific impact of surface free energy on wear resistance depends on various factors, including the type of material, surface roughness, operating conditions (such as load, speed, temperature), and lubrication state.

In practical applications, it is essential to consider surface free energy along with other factors to optimize a material's wear resistance. Calculating surface free energy is vital for understanding and optimizing the surface characteristics of materials. Its impact on wear resistance is complex and can either promote or reduce wear, depending on specific application conditions and material properties. Therefore, a comprehensive consideration of surface free energy and other related factors is necessary for the surface modification of 8Cr4Mo4V bearing steel.

3.7. Coefficient of Friction of Samples Implanted by Different Dose Rates

To assess the impact of dose-rate-enhanced ion implantation on the wear resistance of 8Cr4Mo4V steel, wear tests were performed on both the substrate and samples treated at varying dose rates, as depicted in Figure 7 and Table 4. Notably, the coefficients rise

with increasing dose rates, stabilizing for the as-received sample and those implanted at rates of 7.85×10^{17} ions/cm²·h and 1.04×10^{18} ions/cm²·h. On the contrary, the friction coefficients are lower and vary smoothly with sliding distance for the samples implanted with the dose rates of 2.60×10^{17} ions/cm²·h and 5.18×10^{17} ions/cm²·h. Especially, it is worth mentioning that the coefficient of the dose rate of 1.04×10^{18} ions/cm²·h tends to increase to 0.9 with the testing duration although the coefficient value is better than the untreated sample at the beginning. The initially lower value can be attributed to the enhancement of surface hardness, primarily resulting from the precipitation of Fe₂N and Fe₃N phases.

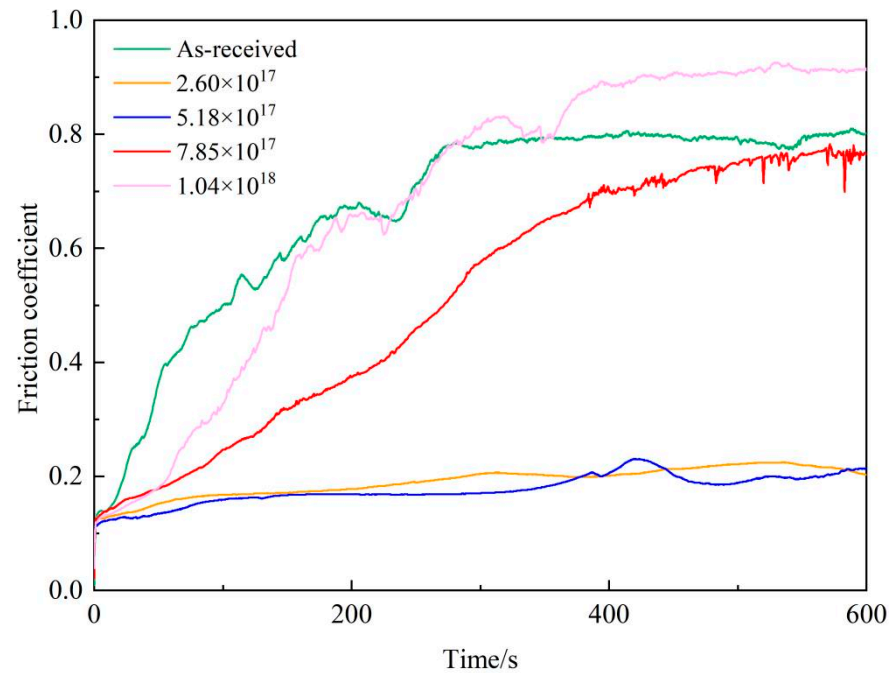


Figure 7. The time dependence in friction coefficient of samples subjected to different dose rates.

Table 4. Average coefficient of friction value of different samples.

Dose rate (ions/cm ² ·h)	0 (As-received)	2.60×10^{17}	5.18×10^{17}	7.85×10^{17}	1.04×10^{18}
Average friction coefficient	0.670	0.191	0.177	0.513	0.681

The maximum average friction coefficient of 0.681 is found for the dose rate of 1.04×10^{18} ions/cm²·h, while the minimum coefficient value of 0.177 is achieved for the dose rate of 5.18×10^{17} ions/cm²·h, which is much lower and relatively stable in contrast with the untreated samples and implanted with other dose rates.

3.8. Wear Behavior Analysis of Samples Implanted by Different Dose Rate

Micrographs of the wear tracks on 8Cr4Mo4V steel plasma treated at different dose rates are shown in Figures 8 and 9. As depicted in Figure 8a, the original specimen and the one enhanced with a dose rate of 1.04×10^{18} ions/cm²·h both exhibit pronounced wear, characterized by deep scratches and debris on their wear tracks. This indicates significant debris removal during the wear test. Conversely, specimens subjected to dose-rate-enhanced ion implantation at rates ranging from 2.60×10^{17} to 7.85×10^{17} ions/cm²·h display smoother and more confined wear scars. The maximum wear scar dimension initially reduces from 302.76 μ m to 144.13 μ m but later rises to 414.02 μ m as the dose rate increases. Notably, the specimen enhanced at 7.85×10^{17} ions/cm²·h possesses the slenderest wear track and demonstrates the least wear loss and rate, a decline of 52.4%,

86.8% and 89.2%, respectively, compared to untreated specimens from Figure 9. This performance is largely attributed to its dominant ϵ -Fe₂₋₃N phase constitution, superior surface hardness, and minimal friction coefficient. As such, specimens implanted at optimal dose rates exhibit diminished wear and a notably lower friction coefficient, pointing to enhanced wear resistance.

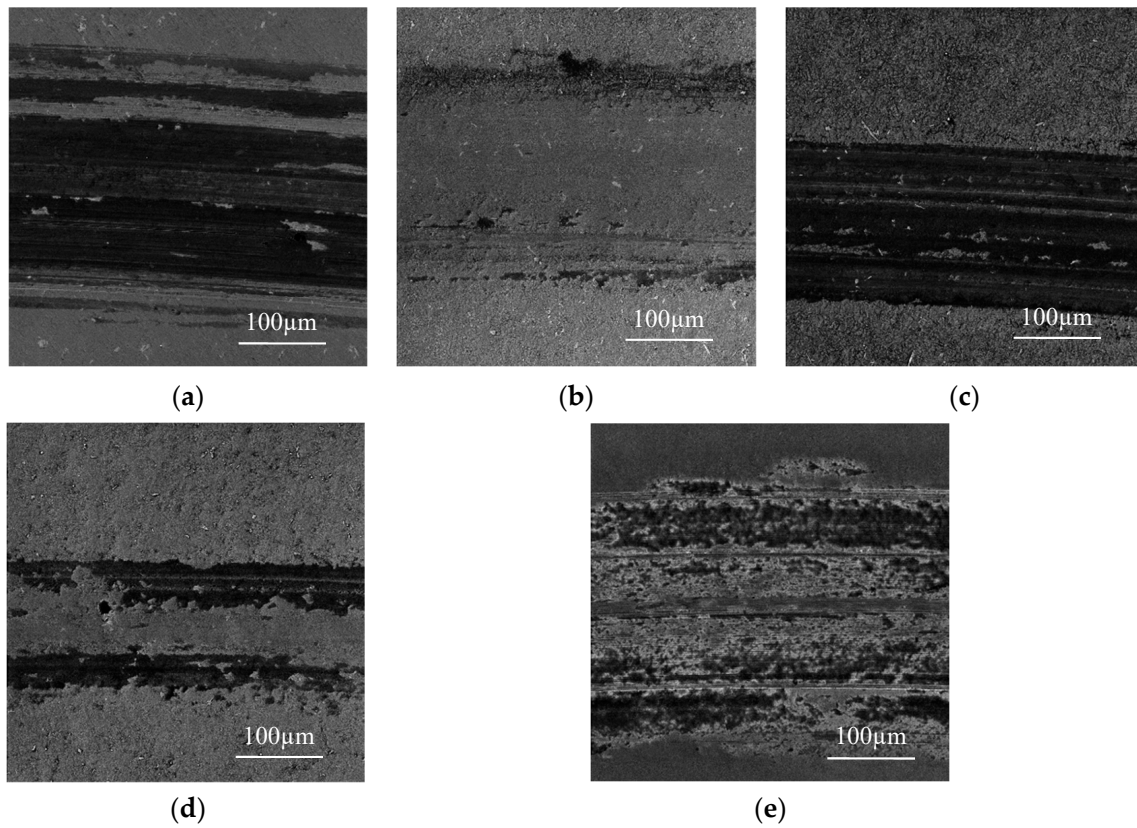


Figure 8. Wear behaviors of samples subjected to different dose rates, (a–e) wear morphology of as-received, 2.60×10^{17} ions/cm²·h, 5.18×10^{17} ions/cm²·h, 7.85×10^{17} ions/cm²·h, 1.04×10^{18} ions/cm²·h, respectively.

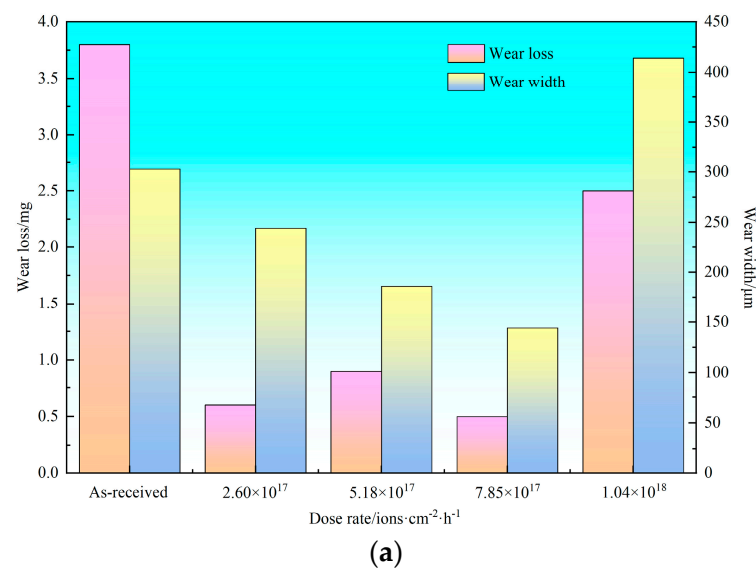


Figure 9. Cont.

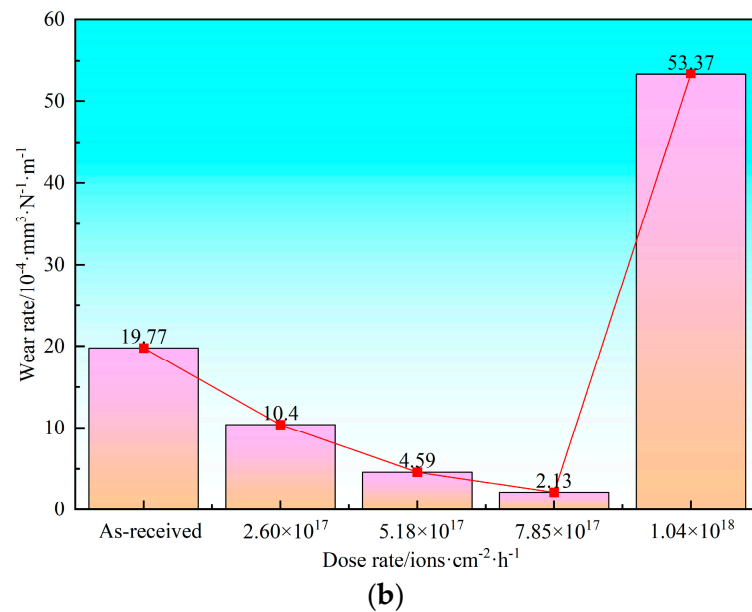


Figure 9. Wear behaviors of samples subjected to different dose rates, (a) wear loss and width, (b) wear rate.

4. Mechanism Discussion

The results clearly suggest that the high-dose-rate treatment significantly enhances the efficiency of plasma immersion ion implantation in 8Cr4Mo4V bearing steel, leading to a marked improvement in its tribological properties.

A comparison with high dose and high intensity implantation methods reported in references [52–54] confirms that this treatment yields optimal enhancements in implantation efficiency and material properties.

The above-mentioned results show that the high-dose-rate nitrogen plasma immersion ion implantation can not only improve the ion implantation efficiency of 8Cr4Mo4V bearing steel but also the wear resistance. These procedures are commonly referred to as radiation modification of materials. Continuous and high-energy ion bombardments inevitably elevate the sample temperature throughout the treatment. This temperature influence on implanted samples is pivotal in the ion implantation process. Figure 1 illustrates the temperature trends for samples implanted at various dose rates, revealing a direct relationship between temperature and dose rate. Specifically, when compared to the samples treated at a dose rate of 2.60×10^{17} ions/cm²·h, the samples exposed to the peak dose rate of 1.04×10^{18} ions/cm²·h experienced a significant temperature rise to approximately 423 °C, an increment of 77 °C. This temperature variation remains consistent, with an error margin below 10%. During the process of high-dose-rate ion implantation, increased ion current densities enable a more intense penetration of ions into the samples.

Upon colliding with sample atoms, these ions transfer their energy, resulting in atom displacement and subsequent radiation defect formation. Additionally, when these ions collide with the target, their trajectories alter, thus causing them to decelerate and embed within the samples at specific depths.

It can be known that the lattice parameters of microstrain and dislocation density are able to reach the highest level of 7.716×10^{-3} and $1.559 \times 10^{16}/\text{m}^2$, respectively, and the crystallite size can reach the smallest value of 11.78 nm at an optimum dose rate of 5.18×10^{17} ions/cm²·h [41]. Unfortunately, the microstrain and dislocation density tend to reduce with the increasing dose rate, which is due to the higher temperature. An infinite increase in the dose rate may initiate a chain reaction, resulting in elevated temperatures in the implanted samples. This can compromise the sample's surface integrity. Conversely, excessively low implantation dose rates can hamper the intended outcomes,

leading to reduced efficiency. Therefore, regulating the implantation dose rate to control the temperature is crucial.

The depth distribution of nitrogen in the samples holds practical significance. An optimal dose rate positively influences the nitrogen concentration on the surface. However, during high-dose-rate ion implantation, the elevated temperatures lead to a reduced surface nitrogen concentration. This reduction is attributed to the diffusion of nitrogen into the matrix, allowing for deeper penetration of the implanted nitrogen atoms.

The dependence of the implanted surface's hardness on implantation temperature is significant. While the surface hardness of 8Cr4Mo4V steel improves compared to the original steel, an intriguing observation is its decrease with rising dose rates. The elevated temperature accelerates the nitrogen diffusion into the matrix core. Concurrently, lattice defects create additional pathways for this inward nitrogen diffusion and the combined effects of these defects and diffusion result in reduced surface hardness but augmented core hardness [55]. The samples implanted at the dose rate of 2.60×10^{17} ions/cm²·h and 5.18×10^{17} ions/cm²·h have the smoothest and lowest friction coefficient; the later dose rate has the narrower wear scar and relatively low wear rate, which is due to the high hardness obtained after this treatment. The decrease in friction coefficient indicates less resistance of relatively moving surfaces of the sample surface and ball, thus decreasing the wear rate. It is well worth noticing that the samples implanted at the dose rate of 7.85×10^{17} ions/cm²·h have a high friction coefficient but a narrow wear width and low wear rate, which is mainly due to the presence of CrN which can not be detected by XRD but is demonstrated in elemental percentage, this phase increases with the increase in implantation dose rate. The protective CrN prevents the detachment of hard abrasive particles from the implanted sample, and thus the friction coefficient is lower and smoother. Despite being implanted at the highest dose rate of 1.04×10^{18} ions/cm²·h, the wear performance of these samples is inferior compared to the as-received samples. This decline in tribological properties is primarily attributed to the minimal presence of iron nitrides and a lower dislocation density in the surface layer. Concurrently, the implanted surface layer is thin and lacks sufficient robustness to withstand prolonged sliding under these conditions. As the testing progresses, the testing ball eventually makes contact with the underlying 8Cr4Mo4V substrate. This interaction results in a sustained coefficient of friction, leading to the generation of more debris and grooves, which in turn, contributes to the observed severe wear resistance during the wear testing. However, the layer implanted on the samples is thin and not strong enough to bear a long time sliding.

In fact, tribological resistance enhancement is a comprehensive action of change that involves hardness, temperature, matrix, grain boundary strengthening and dislocation strengthening. Therefore, it is reasonable to conclude that an optimal dose rate in 8Cr4Mo4V steel ion implantation is beneficial to bringing about higher surface hardness, and thus better wear resistance can be achieved.

5. Conclusions

In the present study, the high-dose-rate plasma immersion ion implantation with nitrogen ions was performed, and the influence of high-dose-rate of implanted 8Cr4Mo4V bearing steel on hardness, structural and tribological properties, and the main following outcomes are obtained:

1. High-dose-rate ion implantation had a significant efficiency on 8Cr4Mo4V bearing steel.
2. For the implanted samples with the different dose rates of 2.60×10^{17} ions/cm²·h, the roughness of Ra decreases from 24.8 nm to 10.4 nm, which is decreased by 58.1% for the dose rates of 7.85×10^{17} ions/cm²·h.
3. The nanohardness of implanted samples improved notably as well, especially in the dose rate of 5.18×10^{17} ions/cm²·h, which reaches a higher value of 16.3 GPa, accompanied by an enlarged hardened region.

4. For the implanted samples, the smallest and highest contact angles of 76.8° and 82.4° are obtained at the dose rate of 7.85×10^{17} ions/cm²·h and 1.04×10^{18} ions/cm²·h, respectively.
5. The wear resistance was greatly improved by an optimal dose rate ion implantation, accompanied by reduced wear weight loss and lower coefficient of friction compared with those without high-dose-rate ion implantation.

Author Contributions: B.M.: Conceptualization, Methodology, Validation, Writing—original draft, Investigation, Writing, review and editing. J.N.: Investigation, Methodology. J.G.: Investigation, Experiment, Methodology. Z.D.: Formal analysis. X.Z.: Methodology. X.M.: Supervision, Conceptualization, Funding acquisition, Writing, review and editing. L.W.: Supervision on Tribological Performance. All authors have read and agreed to the published version of the manuscript.

Funding: This research was funded by National Science and Technology Major Project [2017-VII-0003-0096] and Basic Research Project [2020-JCJQ-ZD-155-12].

Data Availability Statement: Data are contained within the article.

Conflicts of Interest: Author Xinghong Zhang was employed by the company AECC Harbin Bearing Co., Ltd. The remaining authors declare that the research was conducted in the absence of any commercial or financial relationships that could be construed as a potential conflict of interest.

References

1. Jiang, H.; Song, Y.; Wu, Y.; Shan, D.; Zong, Y. Macrostructure, microstructure and mechanical properties evolution during 8Cr4Mo4V steel roller bearing inner ring forging process. *Mater. Sci. Eng.* **2020**, *798*, 140196. [[CrossRef](#)]
2. Lu, H.; Su, H.; Mei, C.; Yang, Q.; Xu, Q.; Xiang, D.; Zhou, T. Effects of B, N, Cr and Mo ion implantation on the corrosion resistance of pure iron and its alloys (GCr15 and Cr4Mo4V). *Vacuum* **1989**, *39*, 187–189.
3. Wang, F.; Zhou, C.; Zheng, L.; Zhang, H. Corrosion resistance of carbon ion implanted M50NiL aerospace bearing steel. *Prog. Nat. Sci. Mater. Int.* **2017**, *27*, 615–621. [[CrossRef](#)]
4. Yu, X.; Wei, Y.; Zheng, D.; Shen, X.; Su, Y.; Xia, Y.; Liu, Y. Effect of nano-bainite microstructure and residual stress on friction properties of M50 bearing steel. *Tribol. Int.* **2022**, *165*, 107285. [[CrossRef](#)]
5. Jiang, T.T.; Zheng, Q. Bearing failure impulse enhancement method using multiple resonance band centre positioning and envelope integration. *Measurement* **2022**, *200*, 111623. [[CrossRef](#)]
6. Harris, T.A.; Skiller, J.; Spitzer, R.F. On the fatigue life of M50 NiL rolling bearings. *Tribol. Trans.* **1992**, *35*, 731–737. [[CrossRef](#)]
7. Wei, Y.; Yu, X.; Su, Y.; Wang, Y.; Yan, G.; Yang, Y. Effect of different thermal treatment temperatures on dimensional stability and mechanical properties of M50 steel. *J. Mater. Res. Technol.* **2022**, *17*, 3047–3054. [[CrossRef](#)]
8. Miao, B.; Niu, J.; Zhang, X.; Guo, J.; Ding, Z.; Ma, X.; Wang, L. The effect of efficient high-dose-rate plasma immersion ion implantation on microstructure and properties of 8Cr4Mo4V steel. *Mater. Today Commun.* **2024**, *38*, 107936. [[CrossRef](#)]
9. Xie, X.Y.; Chen, C.; Luo, J. The microstructure and tribological properties of M50 steel surface after titanium ion implantation. *Appl. Surf. Sci.* **2021**, *564*, 150349. [[CrossRef](#)]
10. Essa, F.A.; Elsheikh, A.H.; Yu, J.; Elkady, O.A.; Saleh, B. Studies on the effect of applied load, sliding speed and temperature on the wear behavior of M50 steel reinforced with Al₂O₃ and/or graphene nanoparticles. *J. Mater. Res. Technol.* **2021**, *12*, 283–303. [[CrossRef](#)]
11. Anders, A. *Handbook of Plasma Immersion Ion Implantation and Deposition*; John Wiley & Sons: New York, NY, USA, 2000.
12. Chu, P.K. Progress in direct-current plasma immersion ion implantation and recent applications of plasma immersion ion implantation and deposition. *Surf. Coat. Technol.* **2013**, *229*, 2–11. [[CrossRef](#)]
13. Wollmann, T.; Nitschke, S.; Klauke, T.; Behnisch, T.; Ebert, C.; Füssel, R.; Modler, N.; Gude, M. Investigating the friction, wear and damage behaviour of plain bearing bushes of the variable stator vane system. *Tribol. Int.* **2022**, *165*, 107280. [[CrossRef](#)]
14. Wang, F.; Qian, D.; Mao, H.; He, Y.; Shu, B. Evolution of microstructure and mechanical properties during tempering of M50 steel with Bainite/Martensite duplex structure. *J. Mater. Res. Technol.* **2020**, *9*, 6712–6722. [[CrossRef](#)]
15. Ooi, S.; Bhadeshia, H.K.D.H. Duplex hardening of steels for aeroengine bearings. *ISIJ Int.* **2012**, *52*, 1927–1934. [[CrossRef](#)]
16. Bhadeshia, H.K.D.H. Steels for bearings. *Prog. Mater. Sci.* **2012**, *57*, 268–435. [[CrossRef](#)]
17. Wang, F.; Qian, D.; Hua, L.; Lu, X. The effect of prior cold rolling on the carbide dissolution, precipitation and dry wear behaviors of M50 bearing steel. *Tribol. Int.* **2019**, *132*, 253–264. [[CrossRef](#)]
18. Wang, F.; Du, Y.; Qian, D.; Cao, N.; Hua, L.; Wu, M. A novel route to improve the fatigue properties of aviation M50 steel via tailoring the bainite content and cold deformation. *J. Mater. Res. Technol.* **2022**, *18*, 3857–3871. [[CrossRef](#)]
19. Du, N.; Liu, H.; Cao, Y.; Fu, P.; Sun, C.; Liu, H.; Li, D. In situ investigation of the fracture of primary carbides and its mechanism in M50 steel. *Mater. Charact.* **2022**, *186*, 111822. [[CrossRef](#)]
20. Shao, Z.; Zhu, Y.; Zhang, P.; Cao, Y.; Wang, B.; Xu, Z.; Liu, H.; Gu, X.; Liu, H.; Li, D.; et al. Effect of primary carbides on rolling contact fatigue behaviors of M50 bearing steel. *Int. J. Fatigue* **2024**, *179*, 108054. [[CrossRef](#)]

21. Yang, L.; Xue, W.; Gao, S.; Li, L.; Cao, Y.; Liu, H.; Duan, D.; Li, D.; Li, S. Rolling contact fatigue behaviour of M50 bearing steel with rare earth addition. *Int. J. Fatigue* **2023**, *177*, 107940. [[CrossRef](#)]
22. Zhou, L.; Tang, G.; Ma, X.; Wang, L.; Zhang, X. Relationship between microstructure and mechanical properties of M50 ultra-high strength steel via quenching-partitioning-tempering process. *Mater. Charact.* **2018**, *146*, 258266. [[CrossRef](#)]
23. Zhu, F.; Jiang, D.; Sun, S.; Wu, H.; Zhang, Z.; Wang, J.; Ren, Z. Effect of alternating magnetic field on microstructure evolution and mechanical properties of M50 bearing steel during tempering process. *J. Mater. Res. Technol.* **2023**, *26*, 4516–4525. [[CrossRef](#)]
24. Du, N.; Liu, H.; Cao, Y.; Fu, P.; Sun, C.; Liu, H.; Li, D. Formation mechanism of MC and M₂C primary carbides in as-cast M50 bearing steel. *Mater. Charact.* **2021**, *174*, 111011. [[CrossRef](#)]
25. Li, J.; Zhan, D.; Jiang, Z.; Zhang, H.; Yang, Y.; Zhang, Y. Progress on improving strength-toughness of ultra-high strength martensitic steels for aerospace applications: A review. *J. Mater. Res. Technol.* **2023**, *23*, 172–190. [[CrossRef](#)]
26. Li, W.; Tang, H.; Meng, X.; Shu, K.; Wang, T.; Gu, L.; Wang, L.; Zhang, C. Effects of surface defects on rolling contact fatigue of M50 steel with consideration to both the transgranular and intergranular damage. *Tribol. Int.* **2023**, *188*, 108775. [[CrossRef](#)]
27. Lorenz, S.J.; Sadeghi, F. Rolling contact fatigue performance of M50 steel: A combined experimental and analytical approach to determine life. *Int. J. Fatigue* **2023**, *176*, 107919. [[CrossRef](#)]
28. Hou, X.-Q.; Zhang, Z.; Liu, C.-K.; Tao, C.-H. Formation mechanism and influence of white etching area on contact fatigue spalling of M50 bearing steel. *Eng. Fail. Anal.* **2022**, *139*, 106273. [[CrossRef](#)]
29. Wang, C.; Zhang, C.; Gu, L.; Bi, M.; Hou, P.; Zheng, D.; Wang, L. Analysis on surface damage of M50 steel at impact-sliding contacts. *Tribol. Int.* **2020**, *150*, 106384. [[CrossRef](#)]
30. Yue, X.; Hu, S.; Wang, X.; Liu, Y.; Yin, F.; Hua, L. Understanding the nanostructure evolution and the mechanical strengthening of the M50 bearing steel during ultrasonic shot peening. *J. Mater. Res. Technol.* **2022**, *836*, 142721. [[CrossRef](#)]
31. Dodd, A.; Kinder, J.; Torp, B.; Nielsen, B.R.; Rangel, C.M.; da Silva, M.F. The effect of ion implantation on the fatigue life and corrosion resistance of M50 steel bearings. *Surf. Coat. Technol.* **1995**, *74–75*, 754–759. [[CrossRef](#)]
32. Davim, J.P. *Wear of Advanced Materials*; John Wiley & Sons: New York, NY, USA, 2011.
33. Kang, Q.; Wei, K.; Fan, H.; Liu, X.; Hu, J. Ultra-high efficient novel plasma aluminum-nitriding methodology and performances analysis. *Scr. Mater.* **2022**, *220*, 114902. [[CrossRef](#)]
34. Xu, S.; Cao, Y.; Duan, B.; Liu, H.; Wang, J.; Si, C. Enhanced strength and sliding wear properties of gas nitrided Ti-6Al-4V alloy by ultrasonic shot peening pretreatment. *Surf. Coat. Technol.* **2023**, *458*, 129325. [[CrossRef](#)]
35. Zhang, L.; Peng, H.; Qin, Q.; Fan, Q.; Bao, S.; Wen, Y. Effects of annealing on hardness and corrosion resistance of 60NiTi film deposited by magnetron sputtering. *J. Alloys Compd.* **2018**, *746*, 45–53. [[CrossRef](#)]
36. Ma, X.; Jiang, S.; Sun, Y.; Tang, G.; Sun, M. Elevated temperature nitrogen plasma immersion ion implantation of AISI 302 austenitic stainless steel. *Surf. Coat. Technol.* **2007**, *201*, 6695–6698. [[CrossRef](#)]
37. Chiu, S.; Lee, S.; Wang, C.; Tai, F.; Chu, C.; Gan, D. Electrical and mechanical properties of DLC coatings modified by plasma immersion ion implantation. *J. Alloys Compd.* **2008**, *449*, 379–383. [[CrossRef](#)]
38. Ziegler, J.F. *Ion Implantation Science and Technology*; Yorktown Heights: New York, NY, USA, 1984.
39. Fernandes, B.; Mändl, S.; Oliveira, R.; Ueda, M. Mechanical properties of nitrogen-rich surface layers on SS304 treated by plasma immersion ion implantation. *Appl. Surf. Sci.* **2014**, *310*, 278–283. [[CrossRef](#)]
40. Mohseni, H.; Mensah, B.A.; Scharf, T.W. Sliding wear and rolling contact fatigue behavior of M50 steel coated with atomic layer deposited lubricious oxide nanolaminates. *Wear* **2023**, *522*, 204865. [[CrossRef](#)]
41. Miao, B.; Zhang, J.; Guo, J.; Ma, X.; Wang, L.; Zhang, X. Understanding the microstructure evolution of 8Cr4Mo4V steel under high-dose-rate ion implantation. *Materials* **2023**, *16*, 5876. [[CrossRef](#)]
42. Ebrahimi, M.; Mahboubi, F.; Naimi-Jamal, M.R. Wear behavior of DLC film on plasma nitrocarburized AISI 4140 steel by pulsed DC PACVD: Effect of nitrocarburizing temperature. *Diam. Relat. Mater.* **2005**, *52*, 32–37. [[CrossRef](#)]
43. Wang, B.; Jin, X.; Xue, W.; Wu, Z.; Du, J.; Wu, J. High temperature tribological behaviors of plasma electrolytic borocarbured Q235 low-carbon steel. *Surf. Coat. Technol.* **2013**, *232*, 142–149. [[CrossRef](#)]
44. Yan, C.; Zeng, Q.F.; He, W.J.; Zhu, J. Enhanced surface hardness and tribocorrosion performance of 60NiTi by boron ion implantation and post-annealing. *Tribol. Int.* **2021**, *155*, 106816. [[CrossRef](#)]
45. Xu, Y.; Ma, X.X.; Sun, M.R. Microstructure characteristics of steel M50 implanted with nitrogen by plasma-based ion implantation at elevated temperature. *Nucl. Instrum. Methods Phys. Res.* **2006**, *242*, 374–376. [[CrossRef](#)]
46. Miao, B.; Zhang, X.; Ma, X. Effects of microstructure and nanohardness of 8Cr4Mo4V steel under high-dose-rate N-PIII. *Trans. IMF* **2023**, *101*, 275–280. [[CrossRef](#)]
47. Xu, S.; Ma, X.; Sun, M.; Sun, Y.; Yukimura, K. Structural and electrical characterizations of Si-implanted GaN with a high dose at elevated temperatures. *Mater. Sci. Semicond. Process.* **2022**, *150*, 106945.
48. Vlcek, P.; Cerny, F.; Drahokoupil, J.; Sepitka, J.; Tolde, Z. The microstructure and surface hardness of Ti6Al4V alloy implanted with nitrogen ions at an elevated temperature. *J. Alloys Compd.* **2015**, *620*, 48–54. [[CrossRef](#)]
49. Sarkar, S.; Patra, S.; Gayathri, N.; Banerjee, S. Effect of self-affine fractal characteristics of surfaces on wetting. *Appl. Phys. Lett.* **2010**, *96*, 063112. [[CrossRef](#)]
50. Nouveau, C.; Labidi, C.; Collet, R.; Benlatreche, Y.; Djouadi, M.-A. Effect of surface finishing such as sand-blasting and CrAlN hard coatings on the cutting edge's peeling tools' wear resistance. *Wear* **2009**, *267*, 1062–1067. [[CrossRef](#)]
51. Packham, D.E. Surface energy, surface topography and adhesion. *Int. J. Adhes. Adhes.* **2003**, *23*, 437–448. [[CrossRef](#)]

52. Ryabchikov, A.I.; Sivin, D.O.; Korneva, O.S.; Bozhko, I.A.; Ivanova, A.I. Modification of the microstructure and properties of martensitic steel during ultra-high dose high-intensity implantation of nitrogen ions. *Surf. Coat. Technol.* **2020**, *388*, 125557. [[CrossRef](#)]
53. Jencyk, P.; Jarzabek, D.M.; Lu, Z.; Gadalińska, E.; Levintant-Zayonts, N.; Zhang, Y. Unexpected crystallographic structure, phase transformation, and hardening behavior in the AlCoCrFeNiTi_{0.2} high-entropy alloy after high-dose nitrogen ion implantation. *Vacuum* **2022**, *216*, 110568. [[CrossRef](#)]
54. Wang, F.; Wang, F.; Ding, X.; Gao, M.; Zhang, H. Microstructure evolution and electrochemical properties of carburized CSS-42L steel by high dose carbon ion implantation. *Thin Solid Film.* **2023**, *771*, 139782. [[CrossRef](#)]
55. Lu, Y.; Li, D.; Ma, H.; Liu, X.; Wu, M.; Hu, J. Enhanced plasma nitriding efficiency and properties by severe plastic deformation pretreatment for 316L austenitic stainless steel. *J. Mater. Res. Technol.* **2021**, *15*, 1742–1746. [[CrossRef](#)]

Disclaimer/Publisher’s Note: The statements, opinions and data contained in all publications are solely those of the individual author(s) and contributor(s) and not of MDPI and/or the editor(s). MDPI and/or the editor(s) disclaim responsibility for any injury to people or property resulting from any ideas, methods, instructions or products referred to in the content.